

Algorithm Design and Prototype Validation for Reconfigurable Intelligent Sensing Surface: Forward-Only Transmission

Cheng Luo, *Graduate Student Member, IEEE*, Luping Xiang, *Member, IEEE*, Jie Hu, *Senior Member, IEEE* and Kun Yang, *Fellow, IEEE*

Abstract—Sensing-assisted communication schemes have recently garnered significant research attention. In this work, we design a dual-function reconfigurable intelligent surface (RIS), integrating both active and passive elements, referred to as the reconfigurable intelligent sensing surface (RISS), to enhance communication. By leveraging sensing results from the active elements, we propose communication enhancement and robust interference suppression schemes for both near-field and far-field models, implemented through the passive elements. These schemes remove the need for base station (BS) feedback for RISS control, simplifying the communication process by replacing traditional channel state information (CSI) feedback with real-time sensing from the active elements. The proposed schemes are theoretically analyzed and then validated using software-defined radio (SDR). Experimental results demonstrate the effectiveness of the sensing algorithms in real-world scenarios, such as direction of arrival (DOA) estimation and radio frequency (RF) identification recognition. Moreover, the RISS-assisted communication system shows strong performance in communication enhancement and interference suppression, particularly in near-field models.

Index Terms—Sensing-assisted communication, DOA estimation, software-defined radio (SDR), over-the-air, prototyping.

I. INTRODUCTION

RECONFIGURABLE intelligent surfaces (RIS) represent a promising innovation for future sixth-generation (6G) networks. This technology consists of a planar surface embedded with numerous cost-effective, passive reflecting elements, each capable of independently adjusting the phase and amplitude of incident electromagnetic signals. This unique capability allows for customized optimization to meet specific functional and performance demands, effectively mitigating the challenges posed by complex wireless propagation environments. Consequently, RIS enhances communication and energy transfer efficiency, coverage, and security [1], [2]. Moreover, the introduction of an additional line-of-sight (LoS) channel further improves signal reliability and transmission efficiency.

Cheng Luo and Jie Hu are with the School of Information and Communication Engineering, University of Electronic Science and Technology of China, Chengdu, 611731, China, email: chengluo@std.uestc.edu.cn; hu-jie@uestc.edu.cn.

Luping Xiang is with the State Key Laboratory of Novel Software Technology, Nanjing University, Nanjing 210008, China, and School of Intelligent Software and Engineering, Nanjing University (Suzhou Campus), Suzhou, email: luping.xiang@uestc.edu.cn

Kun Yang is with the School of Computer Science and Electronic Engineering, University of Essex, Colchester CO4 3SQ, U.K., email: kun.yang@essex.ac.uk.

Due to its low power consumption and simplified hardware architecture, RIS has gained widespread studies in integrated sensing and communication (ISAC) systems [3]–[5] and simultaneous wireless information and power transfer (SWIPT) systems [6], [7]. Moreover, their utility extends to various innovative domains, including robust beamforming techniques [8], electromagnetic wave frequency mixing [9], active RIS configurations [10], and localization [11], providing significant advantages in these areas.

However, several challenges remain, particularly in acquiring accurate channel state information (CSI) between the RIS and its associated primary base stations (BS) or users [12]–[14]. The passive nature of RIS components complicates the CSI acquisition process, resulting in increased pilot overhead that scales with the number of RIS elements and users, as highlighted in [15], [16], thereby complicating conventional channel estimation methods.

Recent studies have sought to address these challenges by developing innovative methods for RIS channel estimation. [17] proposes a compressed sensing approach for estimating RIS cascaded channels, significantly reducing the channel overhead. Another novel solution involves placing power sensors behind each RIS element to enable phase-coherent signal superposition at the receiver through interference observation [18]. A location-based information systems have been employed to enhance beamforming strategies, and detailed performance analysis are provided in [19]. Additionally, empirical data has been leveraged to optimize real world RIS precoding and phase adjustments without knowledge of CSI [20]. A recent study further outlines a CSI-free approach for RIS-assisted large-scale wireless energy transfer (WET), efficiently directing energy across spatial domains using a beam rotation strategy [21].

Moreover, numerous studies have focused on sensing-assisted communication, exploring the potential for collaboration on channel estimation through sensing results or using sensing as an alternative to traditional channel estimation methods. This approach presents both new opportunities and challenges. Specifically, limited CSI is utilized for communication and rough sensing during the initial phase. The collected sensing information is then used to enhance both communication and sensing in the subsequent phase [22]. This two-phase ISAC transmission protocol for RIS-aided MIMO ISAC systems enables cooperative operation between the two functions. Similarly, [23] presents two deep learning

TABLE I
RELEVANT WORKS ON RIS-ASSISTED COMMUNICATION WITH SENSING.

	Sensing scheme	Interference suppression	Robust design	Implementation
Our Proposed	DoA estimation, signal detection	✓	✓	✓
GPS-based [19]	GPS location	✗	✗	✗
Two-phase scheme [22]	Two-phase sensing	✗	✗	✗
Two-network scheme [23]	Radar sensing	✗	✗	✗
RISS-based [24]	DoA estimation	✗	✓	✗

networks designed for beam selection and power allocation, respectively. With the assistance of sensing data, these networks work together to maximize the communication channel capacity. Furthermore, [24] employs both active and passive elements for communication. Specifically, the active elements are utilized to sensing the directions of the BS and users in the uplink and downlink, respectively. The sensing results are then applied to facilitate uplink wireless information transfer (WIT) and downlink WET. Partial related works are presented in Table I.

As a step ahead from [24], we propose a communication enhancement scheme by sensing, including target enhancement and robust interference suppression. And then we design the hardware of RISS for evaluation. Our contributions are summarized as follows:

- We design a dual-functional RIS, which involving active elements and passive elements, termed the reconfigurable intelligent sensing surface (RISS). Thus, the RISS has the ability of sensing and signal processing from active elements. Leveraging this capability, the RISS eliminates the need for base station (BS) control and simplifies traditional CSI feedback by utilizing real-time sensing information. As a result, the proposed system can operate in a purely forward transmission process.
- As the substitution of CSI, we use the sensing information including direction of arrival (DOA) estimation and identification recognition results for RISS passive beamforming design under near-field and far-field channel models. This approach not only enhances the target signal but also suppresses interference, leading to an improved signal-to-interference plus noise ratio (SINR) at the receiver.
- To further evaluate performance, we developed the hardware for the RISS, which includes a 2-bit RIS with 100 passive elements and a uniformly linear array (ULA) with 4 active elements. We implemented two sensing algorithms—DOA estimation and RF identification recognition—as well as the communication system using software-defined radio (SDR). Extensive experiments were conducted to validate the performance of the proposed target enhancement and interference suppression schemes by leveraging the sensing results. The findings demonstrate its effectiveness and provide a strong foundation for future research on advanced communication schemes and sensing beamforming design.

The remainder of this paper is organized as follows: Section II presents an overview of the system model, covering both the near-field and far-field models. Section III discusses the fundamentals of sensing-assisted communication. The hardware and

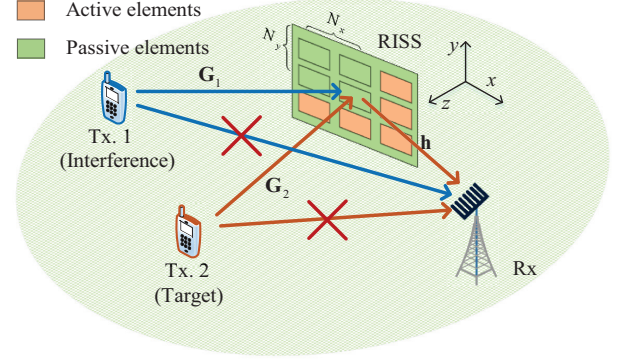


Fig. 1. System model of proposed RISS-assisted communication scheme. The RISS is composed of both active and passive elements.

experimental details are provided in Section IV. Experimental results are outlined in Section V, followed by the findings and conclusions in Section VI.

Notation: \mathbf{I}_M denotes the $M \times M$ identity matrix, and $\mathbf{1}_M$ represents the $M \times 1$ column vector of all ones. The notation $[\cdot]_i$ refers to the i -th element of a vector, while $[\cdot]_{i,j}$ denotes the (i, j) -th element of a matrix. The imaginary unit is represented by $\mathbf{j} = \sqrt{-1}$. The Euclidean norm is denoted by $\|\cdot\|$, and the absolute value is denoted by $|\cdot|$. The function $\text{diag}(\cdot)$ constructs a diagonal matrix. The operators $(\cdot)^T$ and $(\cdot)^H$ denote the transpose and conjugate transpose, respectively. Finally, \mathcal{CN} indicates the circularly symmetric complex Gaussian distribution.

II. SYSTEM MODEL

Far-field and near-field channel models are both adopted for our system in this paper. We assume two M antenna transmitters (Tx) transmit signal simultaneously to a single antenna receiver (Rx) via the RISS, which consists of total $(N_a + N)$ elements, including N_a active elements and $N = N_x \times N_y$ passive elements, as depicts in Fig. 1. We assume these active elements involve the RISS have the ability of signal processing, e.g., DOA estimation and identification recognition. This enables the RISS to operate independently of the BS, eliminating the need for feedback control from the Rx (as shown in Fig. 1), and allows the passive phase shift matrix of RISS to be designed based on sensing information, without relying on traditional CSI feedback. Additionally, there is no direct link between the Rx and Tx.1 and Tx.2 due to blockages, without loss of generality.

A. Far-field Model

Quasi-static block line-of-sight (LoS) channels are taken into account. Specifically, the channel between the Tx-to-RISS and RISS-to-Rx are denoted as $\mathbf{G}_i \in \mathbb{C}^{N \times M}$, $\forall i = \{1, 2\}$ and $\mathbf{h} \in \mathbb{C}^{N \times 1}$, then we have

$$\mathbf{G}_i = \sqrt{MN} \boldsymbol{\alpha}(\vartheta_{G,i}, \varphi_{G,i}) \boldsymbol{\beta}^T(\varpi_{G,i}), \forall i \in \{1, 2\}, \quad (1)$$

$$\mathbf{h} = \sqrt{N} \boldsymbol{\alpha}(\vartheta_h, \varphi_h), \quad (2)$$

$$[\boldsymbol{\alpha}(\vartheta, \varphi)]_n = \frac{1}{\sqrt{N_y}} e^{(\text{mod}(n, N_y) - 1) i \varphi} \frac{1}{\sqrt{N_x}} e^{(\lfloor n/N_x + 1 \rfloor - 1) i \vartheta}, \quad (3)$$

$$[\boldsymbol{\beta}(\varpi)]_n = \frac{1}{\sqrt{M}} e^{(n-1) i \varpi}, \quad (4)$$

where $\varphi = 2\pi d \cos(\phi^{\text{azi}})/\lambda = \pi \cos(\phi^{\text{azi}})$ by setting $d/\lambda = 1/2$ without loss of generality, d and λ represent the element spacing and carrier wavelength, respectively. Similarly, we express $\vartheta = \pi \sin(\phi^{\text{azi}}) \cos(\phi^{\text{ele}})$ and $\varpi = \pi \sin(\phi^{\text{dep}})$. The notation $\text{mod}(\cdot)$ represents the remainder operation, and $\lfloor \cdot \rfloor$ denotes the rounding down operation. Additionally, $\phi_{G,i}^{\text{azi}}$ ($\phi_{G,i}^{\text{ele}}$) and $\phi_{G,i}^{\text{dep}}$ denote the azimuth (elevation) angle of arrival (AOA) and the angle of departure (AOD) from the transmitter to the RISS (Tx-to-RISS). Furthermore, ϕ_h^{azi} (ϕ_h^{ele}) represent the azimuth (elevation) angle of departure (AOD) from the RISS to the receiver (RISS-to-Rx), respectively, as depicts in Fig. 1. Thus, the received signal at the Rx can be formulated as

$$y_F = \sum_{i=1}^2 \sqrt{\varrho_{\text{Tx2R},i} \varrho_{\text{R2Rx}}} \mathbf{h}^T \boldsymbol{\Theta} \mathbf{G}_i \mathbf{v}_i s_i + n_z, \quad (5)$$

where $\varrho_{\text{Tx2R},i}$ and ϱ_{R2Rx} denote the path loss between the Tx to the RISS and the RISS to the Rx, respectively. $\mathbf{v}_i, \forall i \in \{1, 2\}$ denotes the transmit beamforming vector. $\boldsymbol{\Theta} = \text{diag}\{\phi_1, \dots, \phi_N\} \in \mathbb{C}^{N \times N}$ denotes the reflection coefficient matrix of RISS and $|\phi_i| = 1, \forall i \in N$ without loss of generality. $s_i, \forall i \in \{1, 2\}$ is the i^{th} normalized signal, i.e., $\mathbb{E}\{s_i^H s_i\} = 1$. $n_z \sim \mathcal{CN}(0, \sigma_0^2)$ is the additive Gaussian noise.

B. Near-field Model

We denote the location of the m^{th} antenna of the i^{th} Tx as $\mathbf{b}_{\text{Tx},i,m} \in \mathbb{R}^{3 \times 1}, \forall i \in \{1, 2\}, m \in M$ under a three-dimensional (3D) Cartesian coordinate system, while $\mathbf{b}_{\text{Rx}} \in \mathbb{R}^{3 \times 1}$ and $\mathbf{b}_{\text{RISS},k} \in \mathbb{R}^{3 \times 1}, \forall k \in N$ denote the location of Rx and the location of k^{th} element of the RISS, respectively. Furthermore, denote the distance between the $m^{\text{th}}, m \in M$ antenna of the i^{th} Tx and the k^{th} element on the RISS as $d_{\text{Tx2R}}^{i,m,k}, \forall i \in \{1, 2\}, k \in N$, and the distance between the k^{th} element and the Rx as $d_{\text{R2Rx}}^k, \forall k \in N$. We have

$$d_{\text{Tx2R}}^{i,m,k} = \|\mathbf{b}_{\text{Tx},i,m} - \mathbf{b}_{\text{RISS},k}\|, \quad (6)$$

$$d_{\text{R2Rx}}^k = \|\mathbf{b}_{\text{RISS},k} - \mathbf{b}_{\text{Rx}}\|. \quad (7)$$

Thus, the corresponding near-field channel [25] can be formulated as

$$[\bar{\mathbf{G}}_i]_{k,m} = \exp\left(\frac{-i2\pi}{\lambda} d_{\text{Tx2R}}^{i,m,k}\right), i \in \{1, 2\}, k \in N, m \in M, \quad (8)$$

$$[\bar{\mathbf{h}}]_k = \exp\left(\frac{-i2\pi}{\lambda} d_{\text{Tx2R}}^k\right), k \in N, \quad (9)$$

where $\bar{\mathbf{G}}_i \in \mathbb{C}^{N \times M}$ and $\bar{\mathbf{h}} \in \mathbb{C}^{N \times 1}$ denote the channel between the Tx to the RISS, and the RISS to the Rx, respectively. λ denote the carrier wavelength. Similarly, we can derive the received signals at the Rx as

$$\begin{aligned} y_N &= \sum_{i \in \{1, 2\}} \sum_{m \in M} \sum_{k \in N} \sqrt{\varrho(d_{\text{Tx2R}}^{i,m,k}) \varrho(d_{\text{R2Rx}}^k)} \\ &\quad \times [\bar{\mathbf{h}}]_k \phi_k [\bar{\mathbf{G}}_i]_{k,m} [\bar{\mathbf{v}}_i]_m + n_z \\ &\stackrel{(a)}{\approx} \sum_{i=1}^2 \sqrt{\varrho_{\text{Tx2R},i} \varrho_{\text{R2Rx}}} \bar{\mathbf{h}}^T \boldsymbol{\Theta} \bar{\mathbf{G}}_i \bar{\mathbf{v}}_i s_i + n_z, \end{aligned} \quad (10)$$

where (a) comes from the approximate that $\varrho(d_{\text{Tx2R}}^{i,m,k}) \approx \varrho_{\text{Tx2R},i}, \forall m \in M, k \in N$ and $\varrho(d_{\text{R2Rx}}^k) \approx \varrho_{\text{R2Rx}}, \forall k \in N$.

Observe from Eq. (5) and Eq. (10) that the far-field and near-field models share similar expressions¹. However, the specific channel expressions (i.e., Eq. (1)-(2) and Eq. (8)-(9)) differ. We will compare the disparities between the two channels through theoretical algorithm design and practical examination in the subsequent sections.

III. RISS-AID COMMUNICATIONS

In this section, we demonstrate the potential of RISS in interference suppression scenarios. We consider a scenario where two transmitters simultaneously transmit communication signals, with one of the transmitters being undesired, denoted as Tx. 1, serving as the interference source, and Tx. 2 as the target source. The RISS employs active elements for sensing and guides the passive elements for reflection, effectively suppressing the interference signal while enhancing the signal-to-interference-noise ratio (SINR) at the Rx.

A. Far-field RISS-Aid Communications

With the assistance of RISS, we gain knowledge about the incident angles of both the interference signal and the target signal. Additionally, leveraging the capabilities of deep learning, signal incident identification can be recognized effectively, as demonstrated in [26]. This recognition allows for the selective passage of signals by designing appropriate phase shift matrix for RISS. Specifically, the power of the incident signals can be reformulated as

¹In practice, when the transmitter and receiver are sufficiently distant from the RISS, electromagnetic waves transition from near-field spherical wave modeling to far-field plane wave modeling, rendering the near-field and far-field models equivalent.

$$\begin{aligned} & \varrho_{\text{Tx2Rx},i} \varrho_{\text{R2Rx}} \left| \mathbf{h}^T \mathbf{\Theta} \mathbf{G}_i \mathbf{v}_i s_i \right|^2 \\ &= \varrho_{\text{Tx2Rx},i} \left| \boldsymbol{\alpha}^T(\vartheta_h, \varphi_h) \mathbf{\Theta} \boldsymbol{\alpha}(\vartheta_{G,i}, \varphi_{G,i}) \boldsymbol{\beta}^T(\varpi_{G,i}) \mathbf{v}_i \right|^2 \\ & \quad , \forall i \in \{1, 2\} \end{aligned} \quad (11)$$

where $\varrho_{\text{Tx2Rx},i} = \varrho_{\text{Tx2Rx},i} \varrho_{\text{R2Rx}}$.

Lemma 1: Observe from Eq. (11) that the optimal transmit beamforming for the i^{th} transmitter can be derived as

$$\mathbf{v}_i = \sqrt{P_i} \frac{\boldsymbol{\beta}^\dagger(\varpi_{G,i})}{\|\boldsymbol{\beta}(\varpi_{G,i})\|}, \quad (12)$$

where P_i is the transmit power.

Proof: Note that Eq. (11) can be divided into two sub-objective, result in

$$\underbrace{\boldsymbol{\alpha}^T(\vartheta_h, \varphi_h) \mathbf{\Theta} \boldsymbol{\alpha}(\vartheta_{G,i}, \varphi_{G,i})}_{\text{The first objective}} \underbrace{\boldsymbol{\beta}^T(\varpi_{G,i}) \mathbf{v}_i}_{\text{The second objective}}. \quad (13)$$

To maximize the second objective, the maximal ratio transmit (MRT) technique is adopted. Thus, the proof is completed. ■

Remark 1: The rationale behind this segmentation is to effectively decouple the transmitter and RISS. Specifically, the transmitter maximizes power in the RISS direction through beamforming, while the RISS utilizes its active elements for sensing and designs a reflection phase shift matrix to determine whether to enhance or suppress the signal. This design preserves the structure and design principles of traditional transceivers, ensuring spatial freedom for the signal at RISS. The proposed scheme enables the isolation of signals in the spatial domain at the RISS end, facilitating spatial filtering.

According to Lemma 1, Eq. (11) can be rewritten as

$$\begin{aligned} & \varrho_{\text{Tx2Rx},i} \left| \boldsymbol{\alpha}^T(\vartheta_h, \varphi_h) \mathbf{\Theta} \boldsymbol{\alpha}(\vartheta_{G,i}, \varphi_{G,i}) \boldsymbol{\beta}^T(\varpi_{G,i}) \mathbf{v}_i \right|^2 \\ &= \varrho_{\text{Tx2Rx},i} \left| \mathbf{c}_i \boldsymbol{\alpha}(\vartheta_{G,i}, \varphi_{G,i}) \right|^2 \\ &= \varrho_{\text{Tx2Rx},i} \mathbf{c}_i \boldsymbol{\alpha}(\vartheta_{G,i}, \varphi_{G,i}) \boldsymbol{\alpha}^H(\vartheta_{G,i}, \varphi_{G,i}) \mathbf{c}_i^H \\ &= \varrho_{\text{Tx2Rx},i} \mathbf{c}_i \mathbf{A}_i \mathbf{c}_i^H \\ &= \varrho_{\text{Tx2Rx},i} \text{trace}(\mathbf{C}_i \mathbf{A}_i), \forall i \in \{1, 2\} \end{aligned} \quad (14)$$

where $\mathbf{c}_i = \sqrt{MP_i} \boldsymbol{\alpha}^T(\vartheta_h, \varphi_h) \mathbf{\Theta}$, $\mathbf{C}_i = \mathbf{c}_i^H \mathbf{c}_i$, $\mathbf{A}_i = \boldsymbol{\alpha}(\vartheta_{G,i}, \varphi_{G,i}) \boldsymbol{\alpha}^H(\vartheta_{G,i}, \varphi_{G,i})$.

Thus, to maximize the target signal power while eliminate the interference signal power, the objective can be expressed as

$$(\text{P1}): \max_{\boldsymbol{\Theta}} \text{trace}(\mathbf{C}_2 \mathbf{A}_2) \quad (15)$$

$$\text{s.t.} \quad \text{diag}(\mathbf{C}_i) = MP_i \mathbf{1}_N, \forall i \in \{1, 2\}, \quad (15a)$$

$$\text{trace}(\mathbf{C}_i) \leq MN P_i, \forall i \in \{1, 2\}, \quad (15b)$$

$$\text{trace}(\mathbf{C}_1 \mathbf{A}_1) = 0, \quad (15c)$$

$$\mathbf{C}_i = \mathbf{c}_i^H \mathbf{c}_i, \forall i \in \{1, 2\}, \quad (15d)$$

$$\mathbf{c}_i = \sqrt{MP_i} \boldsymbol{\alpha}^T(\vartheta_h, \varphi_h) \mathbf{\Theta}, \forall i \in \{1, 2\}, \quad (15e)$$

$$\text{Rank}(\mathbf{C}_i) = 1, \forall i \in \{1, 2\}, \quad (15f)$$

where the objective (P1) is to maximize the target power gain, with Eq. (15a) to Eq. (15c) derived from constraints imposed by the RISS passive phase shift, transmit power,

and interference elimination. Here, P_i represents the transmit power of the i^{th} transmitter, and we set $P_i = P, \forall i \in \{1, 2\}$ for simplification.

According to Lemma 1 and (P1), we can further simplify objective (P1) as

$$(\text{P1.1}): \max_{\boldsymbol{\Theta}_G} \text{trace}(\mathbf{C}_2 \mathbf{A}_2) \quad (16)$$

$$\text{s.t.} \quad \mathbf{c}_i^T = \sqrt{MP} \mathbf{1}_N^T \boldsymbol{\Theta}_G, \quad (16a)$$

$$\text{trace}(\mathbf{C}_1 \mathbf{A}_1) \leq \tau, \quad (16b)$$

$$(15a), (15b), (15d), \quad (16c)$$

where (16a) and (16b) come from the further segmentation of Eq. (13) as

$$\begin{aligned} & \boldsymbol{\alpha}^T(\vartheta_h, \varphi_h) \mathbf{\Theta} \boldsymbol{\alpha}(\vartheta_{G,i}, \varphi_{G,i}) \\ &= \boldsymbol{\alpha}^T(\vartheta_h, \varphi_h) \mathbf{\Theta}_h \mathbf{\Theta}_G \boldsymbol{\alpha}(\vartheta_{G,i}, \varphi_{G,i}) \\ &= \mathbf{1}_N^T \boldsymbol{\Theta}_G \boldsymbol{\alpha}(\vartheta_{G,i}, \varphi_{G,i}), \end{aligned} \quad (17)$$

where $\mathbf{\Theta}_h = \text{diag}(\boldsymbol{\alpha}^\dagger(\vartheta_h, \varphi_h))$. τ is a reasonable threshold to assess the extent of interference suppression.

Note that we have omitted the rank-one constraint in (P1.1) compared to (P1). Therefore, additional steps, such as Gaussian randomization or iterative rank minimization algorithms (IRM), are required for rank-one reconstruction.

Inspired by [27], we utilize IRM algorithm for rank-one recovery. Specifically, we first obtain the solution of (P1.1) and denote it as \mathbf{C}_2^0 . Once $\text{Rank}(\mathbf{C}_2^0) = 1$, the optimal solution $\boldsymbol{\Theta} = \mathbf{\Theta}_h \mathbf{\Theta}_G^0$ is achieved for the original objective (P1). Otherwise, the objective (P1.1) transforms into

$$(\text{P1.2}): \min_{\boldsymbol{\Theta}_G} -\text{trace}(\mathbf{C}_{2,t} \mathbf{A}_2) + \epsilon_t r \quad (18)$$

$$\text{s.t.} \quad \mathbf{c}_i^T = \sqrt{MP} \mathbf{1}_N^T \boldsymbol{\Theta}_G, \quad (18a)$$

$$\text{trace}(\mathbf{C}_1 \mathbf{A}_1) \leq \tau, \quad (18b)$$

$$r \mathbf{I}_{N-1} - \mathbf{V}_t^H \mathbf{C}_{2,t} \mathbf{V}_t \succeq \mathbf{0}, \quad (18c)$$

$$(15a), (15b), (15d), \quad (18d)$$

where \mathbf{V}_t denotes the matrix composed of eigenvectors corresponding to $[\lambda_1, \dots, \lambda_{N-1}]$, and $\lambda_1 < \lambda_2 < \dots < \lambda_N$ represent the ascending eigenvalues of $\mathbf{C}_{2,t}$ in the t^{th} iteration. Note that (P1.2) is a convex optimization problem, which can be solved by standard optimization method, such as the interior-point method. The IRM algorithm based solution is summarized in Algorithm 1.

B. Near-field RISS-Aid Communications

Similar to the far-field model, we employ the RISS to enhance the target signal while suppressing the interference

Algorithm 1 IRM algorithm based solution for (P1.2).**Input:** \mathcal{A}, M, P, τ .**Output:** Optimal solution \mathcal{C}_2 and optimal phase shift matrix Θ .

- 1: Initialize $\epsilon_0 = 4, t = 0, \varsigma = 1.5$
- 2: Obtain the preliminary solution Θ_G^0 from (P1.1);
- 3: **repeat**
- 4: Obtain the matrix \mathbf{V}_t from eigenvalue decomposition;
- 5: Solve the problem (P1.2) and obtain Θ_G^{t+1} and r ;
- 6: $\epsilon_{t+1} = \epsilon_t^\varsigma$;
- 7: $t = t + 1$;
- 8: **until** r reaches a sufficiently small value or reaches the maximum iterations.
- 9: Obtain the optimal solution Θ_G^t from eigenvalue decomposition of \mathcal{C}_2^t .
- 10: Obtain the optimal phase shift matrix by $\Theta = \Theta_h \Theta_G^t$.

signal. Based on the near-field channel model, we can rewrite Eq. (10) as

$$\begin{aligned}
y_N &\approx \sum_{i \in \{1,2\}} \sqrt{\varrho_{\text{Tx2R},i} \varrho_{\text{R2Rx}}} \sum_{m \in M} \sum_{k \in N} [\bar{\mathbf{h}}]_k \phi_k [\bar{\mathbf{G}}_i]_{k,m} [\bar{\mathbf{v}}_i]_m \\
&\quad + n_z \\
&= \sum_{i \in \{1,2\}} \sqrt{\varrho_{\text{Tx2R},i} \varrho_{\text{R2Rx}}} \sum_{m \in M} [\bar{\mathbf{v}}_i]_m \\
&\quad \times \sum_{k \in N} \exp\left(\frac{-\mathrm{j}2\pi}{\lambda} \left(d_{\text{Tx2R}}^{i,m,k} + d_{\text{R2Rx}}^k\right) + \mathrm{j}\varphi_k\right) + n_z, \quad (19)
\end{aligned}$$

where $\phi_k = \exp(\mathrm{j}\varphi_k)$.

To direct attention towards the design of the reflection phase shift, we assume $M = 1$ for simplification in the subsequent content. Thus, the target signal incident the Rx can be simplified as

$$\begin{aligned}
y_2 &= \sqrt{\varrho_{\text{Tx2R},2} \varrho_{\text{R2Rx}}} \\
&\quad \times \sum_{k \in N} \exp\left(\frac{-\mathrm{j}2\pi}{\lambda} \left(d_{\text{Tx2R}}^{2,k} + d_{\text{R2Rx}}^k\right) + \mathrm{j}\varphi_k\right). \quad (20)
\end{aligned}$$

Represent $y_2 / \sqrt{\varrho_{\text{Tx2R},2} \varrho_{\text{R2Rx}}}$ with S_2 , we have

$$S_2 = \sum_{k \in N} \exp\left(\frac{-\mathrm{j}2\pi}{\lambda} \left(d_{\text{Tx2R}}^{2,k} + d_{\text{R2Rx}}^k\right) + \mathrm{j}\varphi_k\right). \quad (21)$$

Similarly we have²

$$S_1 = \sum_{k \in N} \exp\left(\frac{-\mathrm{j}2\pi}{\lambda} \left(d_{\text{Tx2R}}^{1,k} + d_{\text{R2Rx}}^k\right) + \mathrm{j}\varphi_k\right). \quad (22)$$

Thus, we can formulate the objective as maximizing the reflected target signal while minimizing the interference signal

²Disregarding path loss, S_1 and S_2 represent the strengths of the interference signal and the target signal, respectively.

through the design of the reflection phase shift matrix of the RISS, as

$$(P2): \max_{\Theta} S_2 - \eta S_1 \quad (23)$$

$$\begin{aligned}
\text{s.t. } S_i &= \sum_{k \in N} \exp\left(\frac{-\mathrm{j}2\pi}{\lambda} \left(d_{\text{Tx2R}}^{i,k} + d_{\text{R2Rx}}^k\right) + \mathrm{j}\varphi_k\right) \\
&\quad, \forall i \in \{1, 2\}, \quad (23a)
\end{aligned}$$

$$\eta > 0, \quad (23b)$$

where objective (P2) aims to maximize the reflecting power of the target signal while minimizing the reflecting power of the interference signal. The coefficient η is a constant representing the degree of interference suppression. It is noteworthy that (P2) can be effectively solved by an alternating optimization (AO)-based algorithm, approximating the solution by optimizing one phase shift of the N elements at a time while keeping the others constant. This process continues until the objective value in (P2) converges.

In order to facilitate algorithm convergence, we set the initial phase shift matrix as $\eta = 0$, indicating the sole maximization of the reflecting power of the target signal. Observing from Eq. (21), the optimal φ_k should satisfy

$$\begin{aligned}
\varphi_k - \frac{2\pi}{\lambda} \left(d_{\text{Tx2R}}^{2,k} + d_{\text{R2Rx}}^k\right) \\
= \varphi_l - \frac{2\pi}{\lambda} \left(d_{\text{Tx2R}}^{2,l} + d_{\text{R2Rx}}^l\right) + t2\pi, \\
\forall k \in N, \forall l \in N, t = \pm 1, \pm 2, \dots \quad (24)
\end{aligned}$$

Note that Eq. (24) ensures the effective stacking of each link from Tx. 2 to the Rx to maximize receiver power. We can further simplify the expression of Eq. (24) as

$$\varphi_k = 2\pi \left(\frac{d_{\text{Tx2R}}^{2,k} + d_{\text{R2Rx}}^k}{\lambda} - \left\lfloor \frac{d_{\text{Tx2R}}^{2,k} + d_{\text{R2Rx}}^k}{\lambda} \right\rfloor \right) + \varpi, \quad (25)$$

where $\varpi \in [0, 2\pi]$ denotes the flexible variable shared among all passive elements of the RISS. The AO-based algorithm is summarized in Algorithm 2³.

C. Robust Design

To enhance the application potential of the RISS-assisted communication system, we consider sensing errors in this section. Specifically, due to the inherent width of the main-lobe, and the sharpness of nulls demonstrate in Fig. 2, we aim to ensure the maximization of the target signal while simultaneously broadening the suppression of interference signals for robustness.

We assume that the Tx, Rx and the RISS are all on the same plane, and the location of the Rx is perfectly known (i.e., we have the knowledge of \mathbf{b}_{Rx}), while the actual incident angle of the interference signal (i.e., $\phi_{G,1}^{\text{ele}}$) is within

$$\phi_{G,1}^{\text{ele}} \in [\hat{\phi}_{G,1}^{\text{ele}} - \delta, \hat{\phi}_{G,1}^{\text{ele}} + \delta], \quad (26)$$

³Note that the input location information of Algorithm 2 can be directly estimated by the active elements of the RISS, which includes distance estimation [28], [29] and DOA estimation [30]–[33]. In this paper, we assume that the distances between the Tx, Rx, and the center of the RISS are fixed, while varying the angles of incident signals.

Algorithm 2 AO-based solution for (P2).

Input: The location of Tx $\mathbf{b}_{\text{Tx},i,m} \in \mathbb{R}^{3 \times 1}, \forall i \in \{1, 2\}, m \in M$, the location of the RISS $\mathbf{b}_{\text{RISS},k} \in \mathbb{R}^{3 \times 1}$ and the Rx $\mathbf{b}_{\text{Rx}} \in \mathbb{R}^{3 \times 1}, \forall k \in N$, and wavelength λ .

Output: Optimal passive phase shift matrix Θ .

- 1: Calculate the distance $d_{\text{Tx2R}}^{i,k}$ and d_{R2Rx}^k by Eq. (6) and Eq. (7);
 - 2: Obtain the initial phase shift by Eq. (25);
 - 3: **repeat**
 - 4: **for** $k=1:N$ **do**
 - 5: Find the optimal ϕ_k^* that maximizes the objective function (P2) while keeping the other $\{\phi_n\}_{n=1, n \neq k}^N$ fixed;
 - 6: Update $\phi_k = \phi_k^*$;
 - 7: **end for**
 - 8: **until** Converges or reaches the maximum iterations.
-

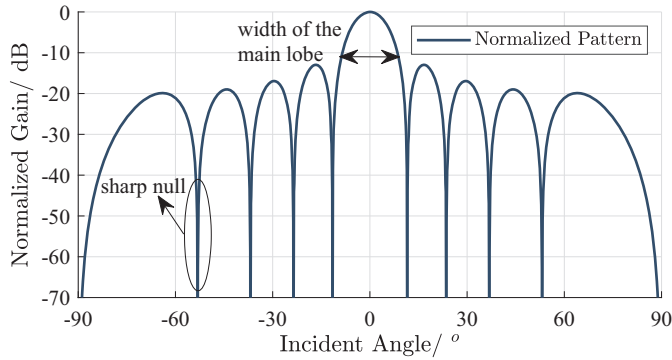


Fig. 2. The reflecting normalized beam pattern, with the main-lobe directed at 0° .

where $\hat{\phi}_{G,1}^{\text{ele}}$ denotes the estimated incident angle of Tx. 1, and $\delta > 0$ represents the boundary of the DOA estimation error. The fundamental robust design approach for both far-field and near-field scenarios involves dividing the interval $[\hat{\phi}_{G,1}^{\text{ele}} - \delta, \hat{\phi}_{G,1}^{\text{ele}} + \delta]$ into L sub-intervals with a step size of $2\delta/(L-1)$, denoted by $\hat{\phi}_{1,l}^{\text{s}}, \forall l \in L$, and applying the suppression constraints to all angles within the interval.

1) *Robust Design for Far-field Model:* Specifically, to broaden the null of the reflecting beam pattern, we apply the constraints (16b) to $\hat{\phi}_{1,l}^{\text{s}}, \forall l \in L$, resulting in

$$(P1.3): \min_{\Theta_G^t} -\text{trace}(\mathbf{C}_{2,t} \mathbf{A}_2) + \epsilon_t r \quad (27)$$

$$\text{s.t. } \text{trace}(\mathbf{C}_1 \mathbf{A}_{1,l}) \leq \tau, \forall l \in L, \quad (27a)$$

$$(16a), (15a), (15b), (15d), \quad (27b)$$

where $\mathbf{A}_{1,l} = \alpha(\hat{\vartheta}_{1,l}^{\text{s}}, \varphi_{G,1}) \alpha^H(\hat{\vartheta}_{1,l}^{\text{s}}, \varphi_{G,1})$, with $\hat{\vartheta}_{1,l}^{\text{s}} = \pi \sin(\pi/2) \cos(\hat{\phi}_{1,l}^{\text{s}})$ due to the assumption that all the Tx, Rx, and the RISS are on the same plane. The IRM algorithm can be continuously used to solve the objective (P1.3) for rank-one recovery.

2) *Robust Design for Near-field Model:* Similar to the far-field scenario, when the actual incident angle of the interference signal is within $\phi_{G,1}^{\text{ele}} \in [\hat{\phi}_{G,1}^{\text{ele}} - \delta, \hat{\phi}_{G,1}^{\text{ele}} + \delta]$, the location of Tx. 1 (i.e., $\mathbf{b}_{\text{Tx},1}$) and the distance between the k^{th} RISS

element and Tx. 1 vary, as depicted in Eq. (6). Thus, the objective (P2) can be rewritten as

$$(P2.1): \max_{\Theta} S_2 - \eta \max\{S_{1,l}\} \quad (28)$$

$$\text{s.t. } d_{\text{Tx2R},l}^{1,k} = \|\mathbf{b}_{\text{Tx},1,l} - \mathbf{b}_{\text{RISS},k}\|, \quad (28a)$$

$$(23a), (23b), \quad (28b)$$

where $S_{1,l} = \sum_{k \in N} \exp\left(\frac{-j2\pi}{\lambda} (d_{\text{Tx2R},l}^{1,k} + d_{\text{R2Rx}}^k) + j\varphi_k\right)$. The detailed solution is outlined in Algorithm 2.

IV. HARDWARE INTRODUCTIONS AND SYSTEM IMPLEMENTS

In this section, we introduce the actual system hardware of the RISS-assisted system, which includes two single horn antenna transmitters (i.e., $M = 1$) and one single horn antenna receiver. Moreover, the RISS consists of $N_a = 4$ active elements for sensing and $N = 100$ passive elements for reflecting.

A. Hardware Introductions

This section introduces the hardware employed within the system and delineates its implementation throughout. Fig. 3 presents an overview of the system's hardware, while Table-II elaborates on the detailed parameters and functions of these hardware components. Note that we utilize an additional external clock (i.e., GPSDO) to synchronize local frequencies across different USRPs.

The hardware of entire system can be divided into three components, including communication component, sensing component and reflecting component.

1) *Communication hardware:* The communication hardware is facilitated by two transmitters and a single receiver. Each transmitter and receiver consists of a USRP paired with a horn antenna, enabling communication via QPSK modulation at $f = 3.5$ GHz.

2) *Sensing hardware:* The sensing hardware consists of two cascaded USRPs and form a $N_a = 4$ RF link linear sensing array receiver.

3) *Reflecting hardware:* The reflecting hardware consists of a single RISS, which involves $N = 100$, $N_a = 4$ and operate at $f = 3.5$ GHz.

B. Communication Model

In this system, we construct two transmitters simultaneously transmitting QPSK signals at 3.5 GHz to the receiver, simulating a scenario with interference present. Our goal is to isolate and receive only one of these signals, treating the signal from the other transmitter as interference. Fig. 4 illustrates the signal's frame structures. It is evident from Fig. 4 that the synchronization head frame serves the purpose of conducting autocorrelation operations at the receiver to determine the start of a frame. To maintain the synchronization head frame's consistency, we incorporate an additional interval frame, separating it from the data frame⁴, resulting in a fixed synchronize

⁴Due to the upsampling and pulse-shaping filter process, the synchronization head frame changes with the data frame. The interval frame ensures a fixed synchronization head independent of the data frame, making it convenient for signal processing and recognition.

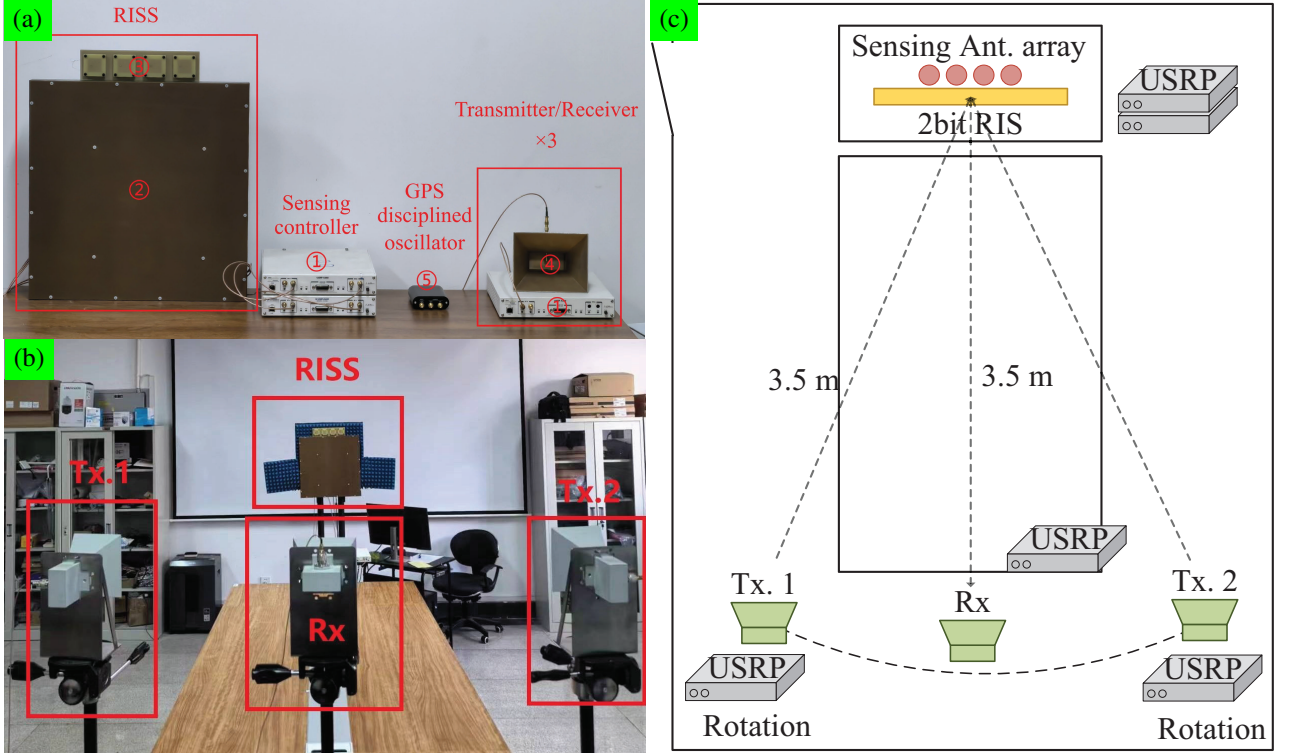


Fig. 3. Experiment measurement setup. (a) The hardware list. (b) Platform units arrangement. (c) Laboratory floor plan.

TABLE II
HARDWARE LIST OF THE ENTIRE SYSTEM.

Num.	Hardware	Size	Parameters and functions
①	Software Defined Radios (SDR)	/	<ul style="list-style-type: none"> USRP X300/X310 series. Each USRP equipped with two UBX-160/SBX-120 series daughter-boards.
②	Reconfigurable Intelligent Surface (RIS)	430 mm (W) × 430 mm (H) × 46 mm (L)	<ul style="list-style-type: none"> 2-bits phase adjustable. 10 × 10 elements. Frequency band 3.4 ~ 3.6 GHz.
③	Sensing Antenna Array	236 mm(W) × 59 mm (H) × 9.2 mm (L)	<ul style="list-style-type: none"> Four elements linear array microstrip antenna. Frequency band 3.08 ~ 3.91 GHz. Total gain 12.6 dBi. Element spacing 0.6883λ, where λ is the wavelength.
④	Horn Antennas	144 mm(W) × 114 mm (H) × 175 mm (L)	<ul style="list-style-type: none"> 10 dB gain horn antenna. Frequency band 2.60 ~ 3.95 GHz.
⑤	GPS Disciplined Oscillator (GPSDO)	70 mm(W) × 24 mm (H) × 130 mm (L)	<ul style="list-style-type: none"> 10MHz SC-Cut High Stability Oven Controlled Crystal Oscillator (OCXO).

head frame and simplify the system. To effectively distinguish between the two transmitted signals, we assign distinct values to the synchronization head frames of each transmitter signal, denoted as $\mathcal{H}_1 = [1, 0, 1, 0, 1, 1, 0, 1, 0, 1, \dots]$ and $\mathcal{H}_2 = [1, 0, 0, 0, 1, 1, 0, 0, 0, 1, \dots]$, while $\tilde{\mathcal{H}}_i \approx \mathcal{H}_i, \forall i = \{1, 2\}$, without loss of generality. And the detailed parameters are summarized in Table-III. Note that $|\mathcal{D}|$ denotes the length of \mathcal{D} , and 5000 bits per frame means that we can transmit 2500 QPSK symbols per frame. R_b and f_s denote the symbol rate and sample rate, respectively.

C. Sensing Model

We emphasize again that our primary aim is to selectively receive the desire signal from the mixed signal through the

TABLE III
THE FRAME STRUCTURE AND PARAMETERS OF COMMUNICATION MODEL

$ \mathcal{D} $	$ \mathcal{H} $	R_b	f_s	Raised cosine filter		
				sps	span	β
5000 bits	500 bits	100 KHz	1.6 MHz	16	16	0.15



Fig. 4. Frame structure of transmitted QPSK signals, where \mathcal{H} , $\tilde{\mathcal{H}}$ and \mathcal{D} denote the synchronize head frame, the interval frame and data frame, respectively.

assistance of sensing. The sensing model comprises two tasks:

DOA estimation and the identification recognition of the two transmitters.

1) *DOA Estimation*: The DOA estimation algorithms based on the linear array have been extensively researched, e.g., Minimum Variance Distortionless Response (MVDR) [30], Multiple Signal Classification (MUSIC) [31], Estimation of Signal Parameters using Rotational Invariance Techniques (ESPRIT) [32], and their variations also have been studied and developed widely. We opt for MUSIC/ROOT-MUSIC algorithm as our DOA estimation scheme after conducting our actual measurement, and we further assume that both transmitter, receiver and RISS are on the same plane. Specifically, while the two signals incident from ϕ_{Tx2R}^1 and ϕ_{Tx2R}^2 , the received signals at the sensing antenna array can be formulated as

$$\mathbf{x}(n) = \mathbf{A}\mathbf{s}(n) + \mathbf{v}(n), \quad (29)$$

where $\mathbf{x}(n) \in \mathbb{C}^{N_a \times 1}$ is the received signals from sensing array at snapshot n , $\mathbf{A} = [\alpha(\phi_{\text{Tx2R}}^1), \alpha(\phi_{\text{Tx2R}}^2)] \in \mathbb{C}^{N_a \times 2}$ is the direction matrix, and $\alpha(\phi_{\text{Tx2R}}^i) = [1, e^{-i\phi_{\text{Tx2R}}^i}, \dots, e^{-i(N_a-1)\phi_{\text{Tx2R}}^i}]^T, \forall i \in \{1, 2\}$ is the direction vectors. $\mathbf{s}(n) \in \mathbb{C}^{2 \times 1}$ and $\mathbf{v}(n) \in \mathbb{C}^{N_a \times 1}$ denote the transmit signals and zero-mean additive white Gaussian noise (AWGN) vector at snapshot n with the normalized noise power σ_0^2 .

Assuming that the two transmitters are statistically independent of each other, thus

$$\mathbb{E}\{s_k(n)s_i^\dagger(n)\} = \begin{cases} P_k, & k = i \\ 0, & k \neq i \end{cases}, \forall i, k \in \{1, 2\}. \quad (30)$$

The covariance matrix of $\mathbf{x}(n)$ is given by

$$\mathbf{R} = \mathbb{E}\{\mathbf{x}(n)\mathbf{x}^H(n)\} = \mathbf{A}\mathbf{P}\mathbf{A}^H + \sigma_0^2\mathbf{I}_{N_a}, \quad (31)$$

where $\mathbf{P} = \mathbb{E}\{\mathbf{s}(n)\mathbf{s}^\dagger(n)\} = \text{diag}\{P_1, P_2\}$, and $P_i, \forall i \in \{1, 2\}$ denotes the average power of the i -th signal.

Following the procedures of the MUSIC algorithm, the eigenvalue decomposition of the matrix \mathbf{R} in Equation (31) is initially derived as

$$\mathbf{R} = [\mathbf{E}_s, \mathbf{E}_z] \begin{bmatrix} \Xi_s & \\ & \Xi_z \end{bmatrix} \begin{bmatrix} \mathbf{E}_s^H \\ \mathbf{E}_z^H \end{bmatrix}, \quad (32)$$

where $\mathbf{E}_s \in \mathbb{C}^{N_a \times 2}$ and $\mathbf{E}_z \in \mathbb{C}^{N_a \times (N_a-2)}$ denote the signal and noise subspaces, respectively, spanned by their corresponding eigenvectors. Ξ_s and Ξ_z denote the corresponding eigenvalues. Due to the orthogonality between $\alpha(\phi_{\text{Tx2R}}^i), \forall i \in \{1, 2\}$ and \mathbf{E}_z , the pseudo spectrum of MUSIC algorithm⁵ can be formulated as

$$P_{\text{MUSIC}}(\phi) = \frac{1}{\alpha(\phi)^H \mathbf{E}_z \mathbf{E}_z^H \alpha(\phi)}, \phi \in [-\pi, \pi]. \quad (33)$$

⁵The ROOT MUSIC [33] algorithm follows a process similar to that of the MUSIC algorithm, with the key distinction lying in the final step, where roots of the equation are sought instead of employing a spectral search as shown in Eq. (33).

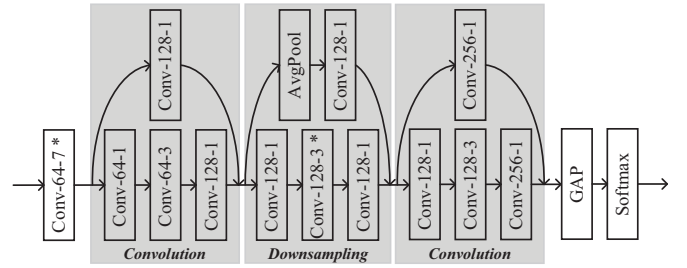


Fig. 5. The structure of SRnet. The layer labeled "Conv-k-s" signifies that this convolutional layer incorporates k kernels, each of size s . All convolutions with a size of 3 are separable. The asterisk (*) indicates that this layer employs a stride of size 2. Batch normalization (BN) is implemented subsequent to each convolution, followed by activation using rectified linear units (ReLUs).

2) *Signal Recognition*: The utilization of signal recognition algorithms plays a pivotal role in identifying incident signals and bolstering network security [34], [35]. In this section, we present a deep-learning-based algorithm, ultimately augmenting the performance of the RISS-assisted system. Specifically, we harness the capabilities of a deep-learning-based algorithm to identify synchronization head frames. This allows us to make informed decisions on whether to enhance or suppress the incident signals⁶.

Fig. 5 illustrates the network architecture we employ for signal recognition, referred to as the signal recognition network (SRnet). The network begins with an initial convolutional layer, followed by a sequence of alternating convolution and downsampling blocks, and concludes with a classification layer. The initial convolutional layer consists of 64 kernels of size 7 with a stride of 2. Both the convolution and downsampling blocks are implemented as residual blocks, inspired primarily by ResNet-B and ResNet-D, as described in [36]. The final classification layer performs global average pooling (GAP) before making predictions via the softmax function. The number of residual blocks can be adjusted to achieve varying levels of modeling capacity. The ResNet used in this study comprises two consecutive convolution blocks, with a downsampling block serving as a transitional stage.

The entire process of the RISS-assisted system is depicted as Fig. 6. Specifically, when the signal is incident on the active elements, DOA information and identity information are recognized and utilized to design the reflected beamforming. The signal is then reflected to the Rx through the passive elements.

V. EXPERIMENT RESULTS

In this section, we practical verify the performance of RISS-assisted system. The entire system including two single horn-antenna Tx (i.e., $M = 1$) and one single horn-antenna Rx, which are both controlled by the USRP X300 and transmit/receive single-carrier QPSK signals, as demonstrated in

⁶RF fingerprint recognition using deep learning has a rich history spanning decades, enabling the extraction of features attributable to hardware defects in transmitter circuits, such as frequency offset and phase shift. This capability facilitates the identification of transmitters. To ensure the system's feasibility, we choose to leverage more prominent features, i.e., the synchronization heads $\mathcal{H}_i, \forall i \in \{1, 2\}$, for the purpose of classification.

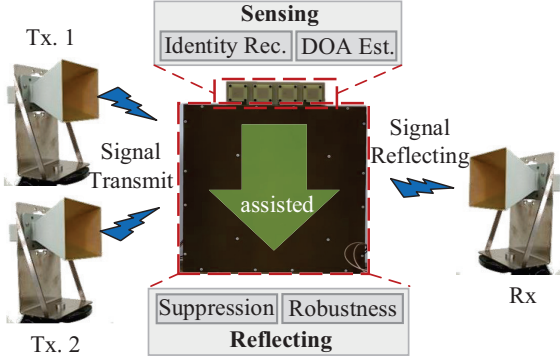


Fig. 6. The entire process of the RISS-assisted system.

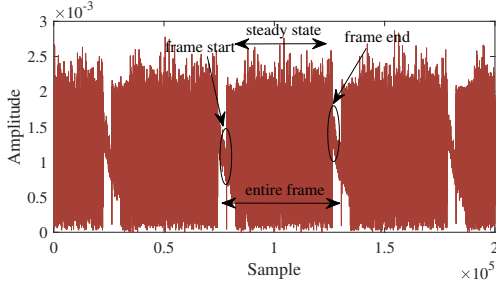


Fig. 7. The amplitude of the samples within a block of USRP sampling varies across the different phases of a frame, which includes the start state, steady state, and end state.

Section IV-A to IV-B. The location of the center of the RISS is set to $[0, 0, 0]$. The distance between Tx/Rx and the center of the RISS is set to $d_c = 3.5$ meters, and the Tx/Rx and RISS are on the same plane, which means that $\phi^{azi} = \pi/2$, thus, the location of the Tx and Rx is set to $\mathbf{b}_{Tx,i} = [d_c \sin(\phi_i^{ele}), 0, d_c \cos(\phi_i^{ele})]$, $\forall i \in \{1, 2\}$ and $\mathbf{b}_{Rx} = [0, 0, d_c]$. In the experiments, we can obtain ϕ_i^{ele} from the DOA algorithm, e.g., MUSIC and ROOTMUSIC, and the identification can be also obtained and determine which Tx is the target source, as depicts in Section IV-C.

A. Sensing Performance

As the foundation of the RISS-assisted system, we first validate the effectiveness of the sensing algorithm. Due to the hardware characteristics, we collect 200000 samples in each USRP sampling block, with each block containing multiple frames. Each frame comprises 48000 samples, including 2,500 information symbols and 500 synchronization head frames, with 16 samples per symbol. For the sake of stability, we pre-process the signal within a USRP sampling block and extract the steady-state segments for DOA estimation, as illustrated in Fig. 7. The snapshot size for MUSIC/ROOTMUSIC DOA estimation is set to 5000 samples.

Fig. 8 demonstrates that both the MUSIC and ROOTMUSIC algorithms can effectively estimate the two incident signals with slight error, thereby enabling more in-depth experimentation.

Table-IV presents parameters and performance of the proposed SR-net. The transmit gains of the two USRPs are

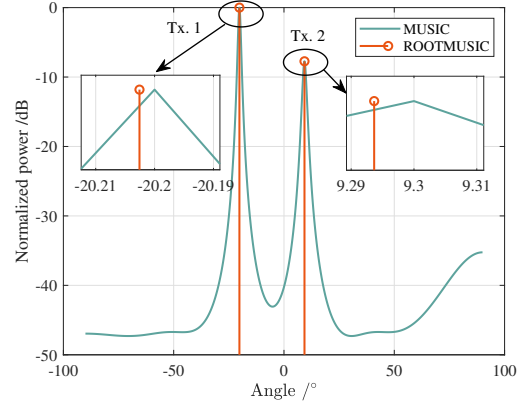


Fig. 8. The experiment results of both MUSIC and ROOTMUSIC implemented by the sensing antenna array within the RISS. The Tx. 1 is located in $\phi_1^{ele} = -20^\circ$ and Tx. 2 is located in $\phi_2^{ele} = 10^\circ$.

TABLE IV
THE PARAMETERS AND PERFORMANCE OF SR-NET.

Dev.	Tx Gain	Actual Tx Power	Blocks	Acc.
Tx. 1	8 dB	-19.46 dBm	100	99.3%
Tx. 2	5 dB	-21.63 dBm		

set to 8 dB and 5 dB, respectively, corresponding to actual transmit powers of -19.46 dBm and -21.63 dBm. A total of 100 sampling blocks are collected and randomly divided into training, validation, and test sets in a 3:1:1 ratio.

Prior to inputting signal samples into SR-net, several pre-processing steps are required:

- 1) DOA estimation: This crucial step involves determining the directions of the incident signals, including both the target and interference signals.
- 2) Spatial filtering: This process is used to separate signals from the combined received data, resulting in distinct samples for the target and interference signals.

Following the pre-processing steps, two signal sets are obtained and used for binary classification with SR-net. The SR-net is implemented using PyTorch [37] and trained on a single NVIDIA RTX A6000 GPU, utilizing the Adam optimizer [38] for 100 epochs. After training the model, it is deployed offline on the upper computer connected to the RISS for sensing.

B. Sensing-assisted Communication for Signal Enhancement

In this section, we first shows the sensing-assisted communication with only one Tx, i.e., $\tau = +\infty$ in Eq. (27) and $\eta = 0$ in Eq. (28) for simplification. This means that our sole objective in this section is to enhance the target signal without considering interference suppression. Fig. 9 demonstrates that RISS enhance the communication performance although the phase shifts of the RISS are not appropriate, since the RISS can increase multipath and change the polarization direction of the signal⁷.

⁷The RISS reverses the polarization, resulting in the polarization of the Tx and Rx being opposite.

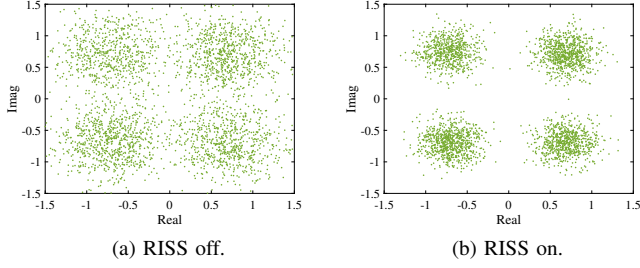


Fig. 9. Constellation diagram measurements of the Rx. (a) Turn off the RISS. (b) Turn on the RISS, but all the phase shifts are set to 0° .

Fig. 10 demonstrates the constellation diagram measurements of the receiver. Note that perfect sensing assumes knowledge of the direction of Tx. 2, i.e., $\phi_2^{\text{ele}} = 10^\circ$. In contrast, imperfect sensing refers to cases where the angle is derived from actual sensing results. As observed in Fig. 10a and 10c, both near-field and far-field models enhance communication performance and significantly improve the SINR at the receiver compared to Fig. 9b. This improvement enables the adoption of higher-order modulation schemes, such as 16QAM and 64QAM, which enhance communication efficiency.

Fig. 10b and Fig. 10d further illustrate that sensing errors have a slight impact on the communication performance of the target signal. This is because the main-lobe possesses an inherent width, as demonstrated in Fig. 2 and discussed in Section III-C. To further illustrate the phenomenon, the normalized beampattern measurements are presented in Fig. 11. Observed from that the main-lobe exhibits robustness for the target signal. Additionally, a side-lobe at -20° is evident in both the near-field and far-field models, which motivates the exploration of robust interference suppression schemes in the following section.

C. Sensing-assisted Communication for Interference Suppression

In this section, we further evaluate the performance of interference suppression. The directions of the target signal and interference signal are set to $\phi_1^{\text{ele}} = -20^\circ$ and $\phi_2^{\text{ele}} = 10^\circ$, respectively. As shown in Fig. 11, the interference signal is located in the side-lobe direction, leading to strong interference at the receiver. Fig. 12 presents the communication constellation diagram with interference suppression using the near-field model, compared to the counterpart scheme that only aligns with the target signal. It can be observed that the interference signal reduces the SINR and causes the constellation diagram to become more dispersed. Furthermore, the constellation diagram exhibits a pattern similar to that of non-orthogonal multiple access (NOMA), due to the power disparity between Tx. 1 and Tx. 2. However, the interference suppression scheme significantly improves the SINR, restoring the compactness of the constellation diagram. The beampatterns of both schemes are shown in Fig. 13. It is important to note that the interference suppression scheme slightly reduces the main-lobe gain

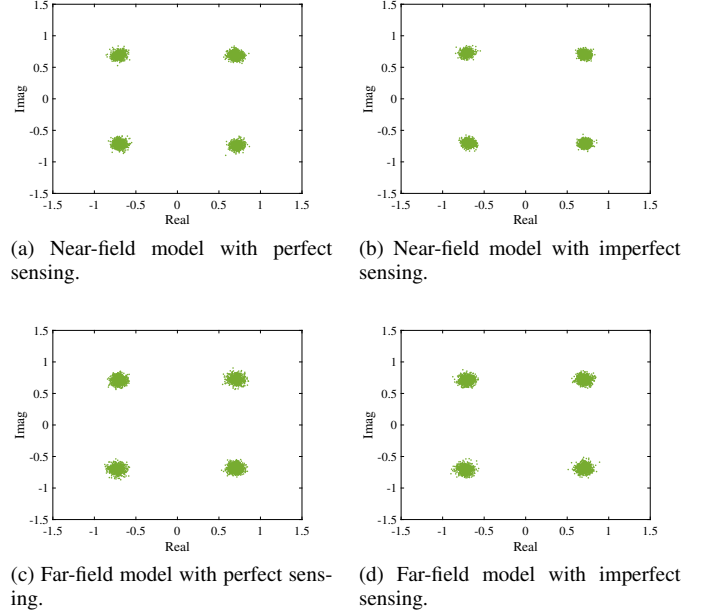


Fig. 10. Constellation diagram measurements of the Rx. (a) Near-field model with perfect sensing. (b) Near-field model with imperfect sensing. (c) Far-field model with perfect sensing. (d) Far-field model with imperfect sensing.

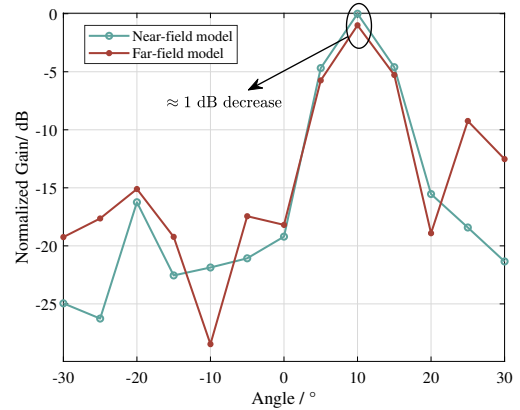


Fig. 11. The normalized beampattern of near-field model and far-field model. The objective of both scheme is to maximize the signal power at the Tx with the knowledge of $\phi_2^{\text{ele}} = 10^\circ$.

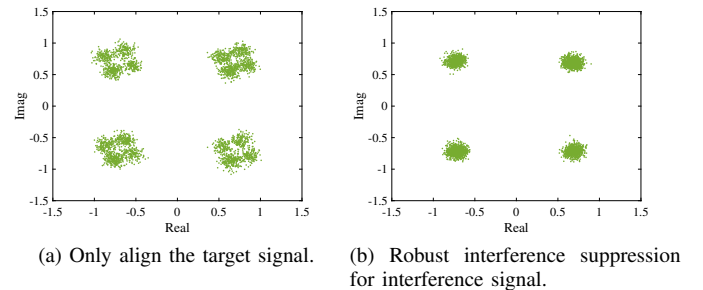


Fig. 12. Constellation diagram measurements of the Rx in near-field model.

while significantly decreasing the side-lobe gain associated with the interference.

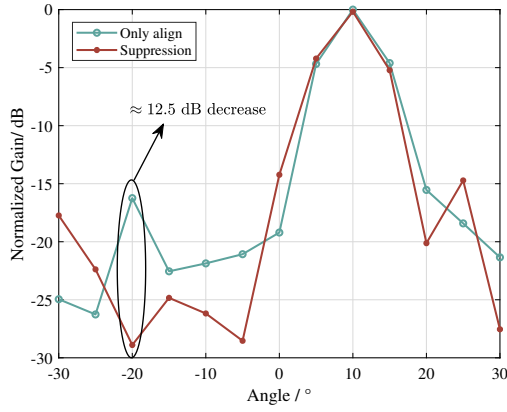


Fig. 13. The beampattern of align scheme and interference suppression scheme in the near-field model. The target signal is located in $\phi_1^{\text{ele}} = -20^\circ$, while the interference signal is located in $\phi_2^{\text{ele}} = 10^\circ$.

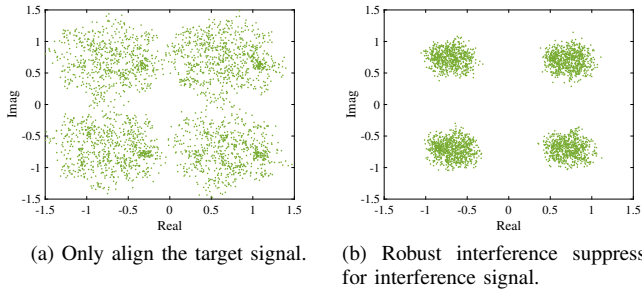


Fig. 14. Constellation diagram measurements of the Rx in far-field model.

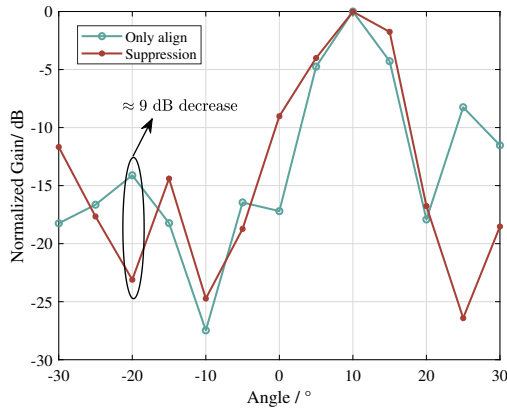
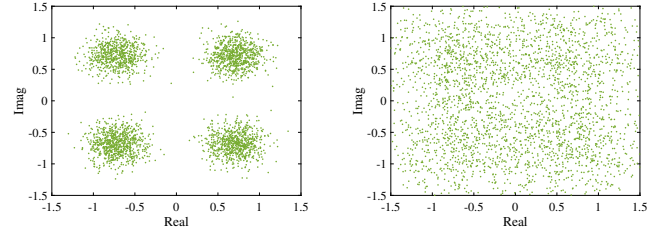


Fig. 15. The beampattern of align scheme and interference suppression scheme in the far-field model. The target signal is located in $\phi_1^{\text{ele}} = -20^\circ$, while the interference signal is located in $\phi_2^{\text{ele}} = 10^\circ$.

In contrast, as illustrated in Fig. 14 and Fig. 15, the interference suppression in the far-field model is weak. This phenomenon may be attributed to the relatively close distance, rendering the far-field model inapplicable, or possibly due to RIS phase errors leading to interference suppression failure.

Finally, to further investigate interference suppression, we deactivate Tx. 2, allowing the receiver to capture only the interference signal. The constellation measurements for both the align scheme and the interference suppression scheme



(a) Interference constellation with only align scheme. (b) Interference constellation with robust interference suppression.

Fig. 16. Constellation diagram measurements of the Rx while only Tx. 2 is available.

using the near-field model are displayed in 16. With only Tx. 1 active, the constellation in 16a shows that the align scheme retains significant interference signal power. In contrast, the interference suppression scheme shows effective interference mitigation, resulting in a highly dispersed constellation diagram of the interference signal, further demonstrating the robustness of the interference suppression technique.

VI. CONCLUSION

This paper introduces a RISS-assisted communication system, with both far-field and near-field models designed for target signal enhancement and robust interference suppression. Leveraging the signal processing ability of active elements, the RISS operates independently, eliminating the need for traditional CSI feedback and enabling a purely forward transmission process. Extensive over-the-air experiments validate the system's sensing capabilities, such as DOA estimation and identification recognition, as well as the effectiveness of the RISS-based communication scheme for signal enhancement and robust interference suppression. While both far-field and near-field models are effective for target enhancement, the near-field model demonstrates superior performance in interference suppression within our experimental setup. The successful validation of this sensing-assisted communication system lays a solid foundation for future research on innovative communication schemes and advanced sensing beampattern designs.

REFERENCES

- [1] Q. Wu, S. Zhang, B. Zheng, C. You, and R. Zhang, "Intelligent reflecting surface-aided wireless communications: A tutorial," *IEEE Transactions on Communications*, vol. 69, no. 5, pp. 3313–3351, 2021.
- [2] Y. Liu, X. Liu, X. Mu, T. Hou, J. Xu, M. Di Renzo, and N. Al-Dhahir, "Reconfigurable intelligent surfaces: Principles and opportunities," *IEEE Communications Surveys & Tutorials*, vol. 23, no. 3, pp. 1546–1577, 2021.
- [3] K. Chen, C. Qi, O. A. Dobre, and G. Y. Li, "Simultaneous beam training and target sensing in isac systems with ris," *IEEE Transactions on Wireless Communications*, vol. 23, no. 4, pp. 2696–2710, 2024.
- [4] K. Zhong, J. Hu, C. Pan, M. Deng, and J. Fang, "Joint waveform and beamforming design for ris-aided isac systems," *IEEE Signal Processing Letters*, vol. 30, pp. 165–169, 2023.
- [5] X. Tong, Z. Zhang, J. Wang, C. Huang, and M. Debbah, "Joint multi-user communication and sensing exploiting both signal and environment sparsity," *IEEE Journal of Selected Topics in Signal Processing*, vol. 15, no. 6, pp. 1409–1422, 2021.

- [6] C. Pan, H. Ren, K. Wang, M. El Kashlan, A. Nallanathan, J. Wang, and L. Hanzo, "Intelligent reflecting surface aided MIMO broadcasting for simultaneous wireless information and power transfer," *IEEE Journal on Selected Areas in Communications*, vol. 38, no. 8, pp. 1719–1734, 2020.
- [7] Q. Wu and R. Zhang, "Joint active and passive beamforming optimization for intelligent reflecting surface assisted SWIPT under QoS constraints," *IEEE Journal on Selected Areas in Communications*, vol. 38, no. 8, pp. 1735–1748, 2020.
- [8] G. Zhou, C. Pan, H. Ren, K. Wang, and A. Nallanathan, "A framework of robust transmission design for IRS-aided MISO communications with imperfect cascaded channels," *IEEE Transactions on Signal Processing*, vol. 68, pp. 5092–5106, 2020.
- [9] J. Zhao, X. Yang, J. Y. Dai, Q. Cheng, X. Li, N. H. Qi, J. C. Ke, G. D. Bai, S. Liu, S. Jin *et al.*, "Programmable time-domain digital-coding metasurface for non-linear harmonic manipulation and new wireless communication systems," *National science review*, vol. 6, no. 2, pp. 231–238, 2019.
- [10] Z. Zhang, L. Dai, X. Chen, C. Liu, F. Yang, R. Schober, and H. V. Poor, "Active RIS vs. passive RIS: Which will prevail in 6G?" *IEEE Transactions on Communications*, vol. 71, no. 3, pp. 1707–1725, 2023.
- [11] M. Hua, Q. Wu, W. Chen, Z. Fei, H. C. So, and C. Yuen, "Intelligent reflecting surface-assisted localization: Performance analysis and algorithm design," *IEEE Wireless Communications Letters*, vol. 13, no. 1, pp. 84–88, 2024.
- [12] Z. Wang, L. Liu, and S. Cui, "Channel estimation for intelligent reflecting surface assisted multiuser communications: Framework, algorithms, and analysis," *IEEE Transactions on Wireless Communications*, vol. 19, no. 10, pp. 6607–6620, 2020.
- [13] C. Hu, L. Dai, S. Han, and X. Wang, "Two-timescale channel estimation for reconfigurable intelligent surface aided wireless communications," *IEEE Transactions on Communications*, vol. 69, no. 11, pp. 7736–7747, 2021.
- [14] N. K. Kundu and M. R. McKay, "Large intelligent surfaces with channel estimation overhead: Achievable rate and optimal configuration," *IEEE Wireless Communications Letters*, vol. 10, no. 5, pp. 986–990, 2021.
- [15] K. Zhi, C. Pan, H. Ren, and K. Wang, "Power scaling law analysis and phase shift optimization of RIS-aided massive MIMO systems with statistical CSI," *IEEE Transactions on Communications*, vol. 70, no. 5, pp. 3558–3574, 2022.
- [16] C. Pan, G. Zhou, K. Zhi, S. Hong, T. Wu, Y. Pan, H. Ren, M. D. Renzo, A. Lee Swindlehurst, R. Zhang, and A. Y. Zhang, "An overview of signal processing techniques for RIS/IRS-aided wireless systems," *IEEE Journal of Selected Topics in Signal Processing*, vol. 16, no. 5, pp. 883–917, 2022.
- [17] P. Wang, J. Fang, H. Duan, and H. Li, "Compressed channel estimation for intelligent reflecting surface-assisted millimeter wave systems," *IEEE Signal Processing Letters*, vol. 27, pp. 905–909, 2020.
- [18] J. Zhu, K. Liu, Z. Wan, L. Dai, T. J. Cui, and H. Vincent Poor, "Sensing RISs: Enabling dimension-independent CSI acquisition for beamforming," *IEEE Transactions on Information Theory*, pp. 1–1, 2023.
- [19] X. Hu, C. Zhong, Y. Zhang, X. Chen, and Z. Zhang, "Location information aided multiple intelligent reflecting surface systems," *IEEE Transactions on Communications*, vol. 68, no. 12, pp. 7948–7962, 2020.
- [20] S. Ren, K. Shen, Y. Zhang, X. Li, X. Chen, and Z.-Q. Luo, "Configuring intelligent reflecting surface with performance guarantees: Blind beamforming," *IEEE Transactions on Wireless Communications*, pp. 1–1, 2022.
- [21] C. Luo, J. Hu, L. Xiang, K. Yang, and K.-K. Wong, "Massive wireless energy transfer without channel state information via imperfect intelligent reflecting surfaces," *IEEE Transactions on Vehicular Technology*, vol. 73, no. 6, pp. 8529–8541, 2024.
- [22] X. Qian, X. Hu, C. Liu, M. Peng, and C. Zhong, "Sensing-based beamforming design for joint performance enhancement of RIS-aided ISAC systems," *IEEE Transactions on Communications*, vol. 71, no. 11, pp. 6529–6545, 2023.
- [23] L. Chen, K. Liu, Z. Zhang, and B. Li, "Beam selection and power allocation: Using deep learning for sensing-assisted communication," *IEEE Wireless Communications Letters*, vol. 13, no. 2, pp. 323–327, 2024.
- [24] C. Luo, J. Hu, L. Xiang, and K. Yang, "Reconfigurable intelligent sensing surface aided wireless powered communication networks: A sensing-then-reflecting approach," *IEEE Transactions on Communications*, pp. 1–1, 2023.
- [25] Y. Han, S. Zhang, L. Duan, and R. Zhang, "Cooperative double-IRS aided communication: Beamforming design and power scaling," *IEEE Wireless Communications Letters*, vol. 9, no. 8, pp. 1206–1210, 2020.
- [26] W. Wang, C. Luo, J. An, L. Gan, H. Liao, and C. Yuen, "Semi-supervised rf fingerprinting with consistency-based regularization," *IEEE Internet of Things Journal*, pp. 1–1, 2023.
- [27] C. Sun, N. Kingry, and R. Dai, "A unified formulation and nonconvex optimization method for mixed-type decision-making of robotic systems," *IEEE Transactions on Robotics*, vol. 37, no. 3, pp. 831–846, 2021.
- [28] C.-H. Chen and K.-T. Feng, "Enhanced distance and location estimation for broadband wireless networks," *IEEE Transactions on Mobile Computing*, vol. 14, no. 11, pp. 2257–2271, 2015.
- [29] N. Salman, M. Ghogho, and A. H. Kemp, "On the joint estimation of the RSS-based location and path-loss exponent," *IEEE Wireless Communications Letters*, vol. 1, no. 1, pp. 34–37, 2012.
- [30] J. Capon, "High-resolution frequency-wavenumber spectrum analysis," *Proceedings of the IEEE*, vol. 57, no. 8, pp. 1408–1418, 1969.
- [31] R. Schmidt, "Multiple emitter location and signal parameter estimation," *IEEE Transactions on Antennas and Propagation*, vol. 34, no. 3, pp. 276–280, 1986.
- [32] R. Roy and T. Kailath, "Esprit-estimation of signal parameters via rotational invariance techniques," *IEEE Transactions on Acoustics, Speech, and Signal Processing*, vol. 37, no. 7, pp. 984–995, 1989.
- [33] A. Barabell, "Improving the resolution performance of eigenstructure-based direction-finding algorithms," in *ICASSP '83. IEEE International Conference on Acoustics, Speech, and Signal Processing*, vol. 8, 1983, pp. 336–339.
- [34] Y. Zou, J. Zhu, X. Wang, and L. Hanzo, "A survey on wireless security: Technical challenges, recent advances, and future trends," *Proceedings of the IEEE*, vol. 104, no. 9, pp. 1727–1765, 2016.
- [35] J. M. Hamamreh, H. M. Furqan, and H. Arslan, "Classifications and applications of physical layer security techniques for confidentiality: A comprehensive survey," *IEEE Communications Surveys & Tutorials*, vol. 21, no. 2, pp. 1773–1828, 2019.
- [36] T. He, Z. Zhang, H. Zhang, Z. Zhang, J. Xie, and M. Li, "Bag of tricks for image classification with convolutional neural networks," in *Proceedings of the IEEE/CVF conference on computer vision and pattern recognition*, 2019, pp. 558–567.
- [37] A. Paszke, S. Gross, F. Massa, A. Lerer, J. Bradbury, G. Chanan, T. Killeen, Z. Lin, N. Gimelshein, L. Antiga *et al.*, "Pytorch: An imperative style, high-performance deep learning library," *Advances in neural information processing systems*, vol. 32, 2019.
- [38] D. P. Kingma and J. Ba, "Adam: A method for stochastic optimization," *arXiv preprint arXiv:1412.6980*, 2014.